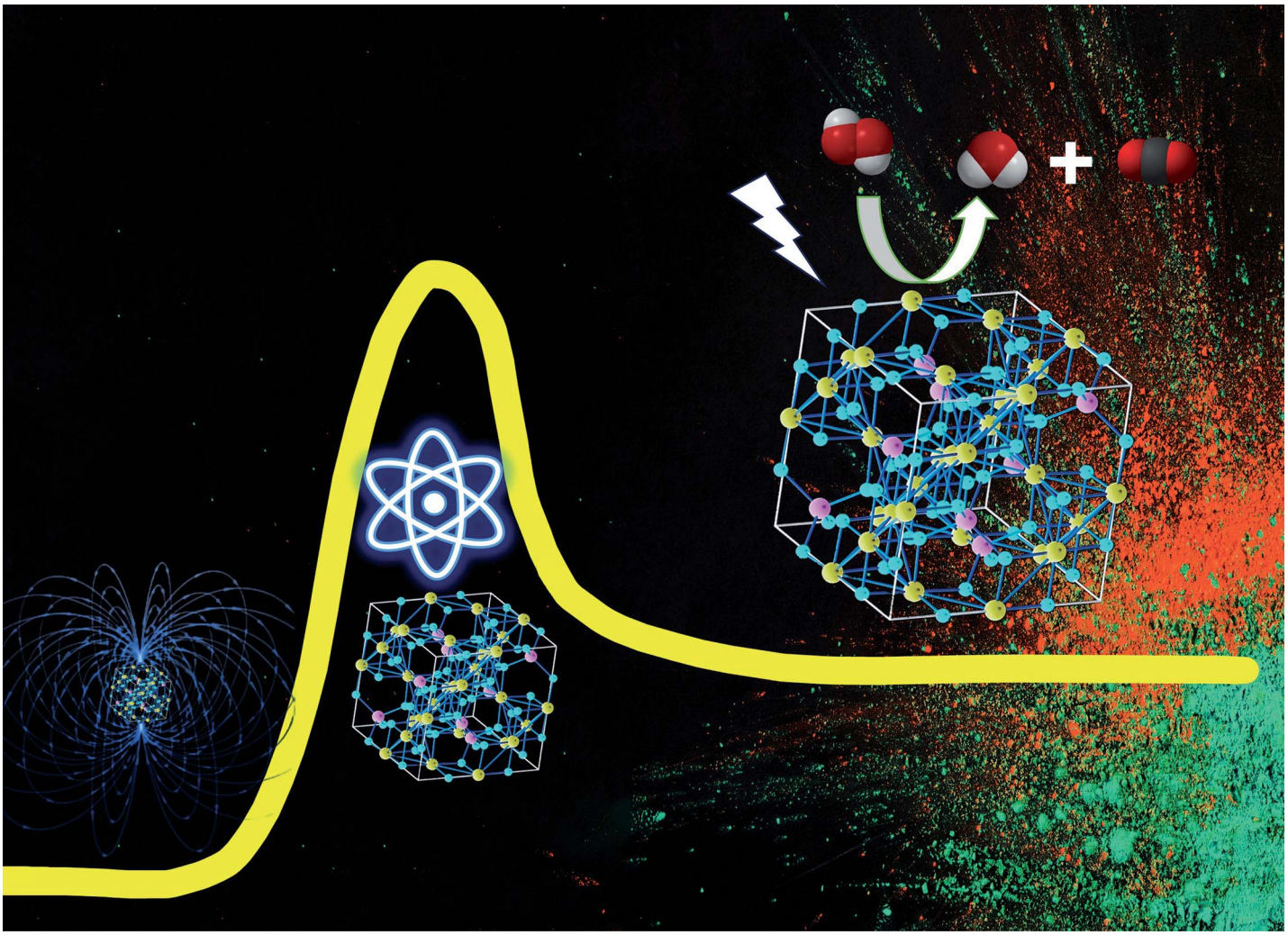

Showcasing research from Professor Chowdhury's laboratory, Material Nanochemistry Laboratory, Institute of Advanced Study in Science and Technology, Guwahati, India.

Nanocrystalline Ni–Zn spinel ferrites: size-dependent physical, photocatalytic and antioxidant properties

Nanostructured $Zn_{0.3}Ni_{0.7}Fe_2O_4$ samples of different particle size were prepared *via* the chemical co-precipitation method. The emergence of superparamagnetic behavior has been observed for the smallest-sized Ni–Zn ferrite nanoparticles. Ni–Zn spinel ferrite nanoparticles also exhibited size-dependent scavenging of free radicals. Additionally, Ni–Zn spinel ferrite nanoparticles demonstrated efficiency as a catalyst in degrading MB dye under light illumination.

As featured in:

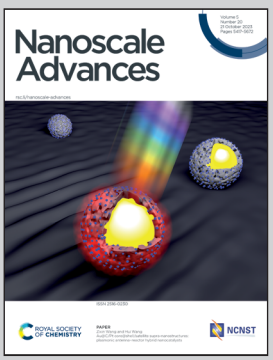

See Mritunjoy Prasad Ghosh, Devasish Chowdhury *et al.*, *Nanoscale Adv.*, 2023, **5**, 5460.

ROYAL SOCIETY OF CHEMISTRY

rsc.li/nanoscale-advances

Registered charity number: 207890

Nanoscale Advances

ROYAL SOCIETY OF CHEMISTRY

PAPER

View Article Online
View Journal | View Issue

Check for updates

Cite this: *Nanoscale Adv.*, 2023, **5**, 5460

Nanocrystalline Ni–Zn spinel ferrites: size-dependent physical, photocatalytic and antioxidant properties†

Nur Jalal Mondal, [ab] Rahul Sonkar, [ab] Bitopan Boro, [ab] Mritunjoy Prasad Ghosh [*a] and Devasish Chowdhury [*ab]

The physical properties of nanomagnetic particles are expected to be highly dependent on their size. In this study, besides the promising applications of nanocrystalline Ni–Zn spinel ferrites in the area of photocatalysis and free radical scavenging, we present a detailed study with appropriate scientific explanations on the role of size change in modifying and tuning the microstructural, optical and magnetic properties. Three nanostructured $Zn_{0.3}Ni_{0.7}Fe_2O_4$ samples of different particle sizes were prepared *via* the chemical co-precipitation method. Crystallographic phase purity and formation of the spinel cubic phase for all the samples were tested by X-ray diffraction studies. The magnetic properties of the as-synthesized ferrite nanoparticles have been examined thoroughly at 5 K and 300 K. Emergence of superparamagnetic behavior has been observed for the sample with the smallest size ferrite nanoparticles (ZNF-1). The photocatalytic efficiency of all the nanocatalysts was tested on methylene blue (MB) dye and the smallest sized nanocatalyst (ZNF-1) was identified as the most efficient catalyst in degrading MB dye under light illumination. The degradation efficiency was found to decrease with increasing mean particle size of the prepared samples. The antioxidant properties of the prepared ferrite samples were also studied. Here, too, the ZNF-1 sample with the smallest sized nanoparticles exhibited maximum scavenging of free radicals compared to other samples. Hence, the present study clearly demonstrates that smaller-sized Ni–Zn spinel ferrites are efficient materials for tuning the physical properties as well as for use in photocatalytic and antioxidant applications.

Received 23rd June 2023
Accepted 25th August 2023

DOI: 10.1039/d3na00446e

rsc.li/nanoscale-advances

Open Access Article. Published on 25 August 2023. Downloaded on 2/6/2026 1:27:51 PM.
This article is licensed under a Creative Commons Attribution-NonCommercial 3.0 Unported Licence.

Introduction

In this decade, wastewater treatment has become a major challenge worldwide to protect the natural sources of water. Due to the turbulent growth of numerous industries, especially in developing countries, for managing human needs, wastewater treatment has actively drawn the attention of researchers.[1–3] Eliminating harmful contaminants from wastewater is extremely necessary due to their terrible long-term environmental impacts. Among different growing industries, the industries that deal with pigments and dyes have become a massive source of wastewater that contains toxic pollutants. The widely used non-biodegradable toxic dyes in textiles, plastic, leather, cosmetics, paper, food and other sectors have actively been producing dye effluents. These toxic dye pollutants can cause crucial environmental and also human health issues if left untreated in wastewater.[1,2] The poisonous nature of dye pollutants may cause damage to the human body's skin, eyes, and respiratory and nervous systems even at low concentrations.[2–5] Therefore, complete removal of deadly organic dyes from wastewater is highly required. Several techniques have been developed for the treatment of dye-containing wastewater in the past few decades. Among them, the photocatalysis process using nanosized catalysts is greatly preferred for degrading toxic organic dyes. Photocatalytic reduction of dyes using nanocatalysts is a simple and cost-effective way in which photogenerated electron–hole pairs due to light irradiation actively participate in the oxidation and reduction process. Nanosized semiconductors having bandgap near 2 eV have become promising candidates for photocatalysts due to their high specific surface area, pore size and surface charge.[4–8] Besides photodegradation using ferrite nanoparticles, the antioxidant properties of nanoferrites have attracted the attention of research communities in recent times. Antioxidant substances inhibit oxidation, reduce free radicals and prevent cell damage.[9–11] Antioxidant qualities in spinel ferrites have been explored extensively in the last two decades.

As most of the spinel cubic ferrites in the nanoscale regime consist of an optical bandgap near the visible range, these

[a]*Material Nanochemistry Laboratory, Physical Sciences Division, Institute of Advanced Study in Science and Technology, Paschim Boragaon, Garchuk, Guwahati 781035, Assam, India. E-mail: mritunjoyprasad92@gmail.com; devasish@iasst.gov.in*

[b]*Academy of Scientific and Innovative Research (AcSIR), Ghaziabad 201002, India*

† Electronic supplementary information (ESI) available. See DOI: https://doi.org/10.1039/d3na00446e

© 2023 The Author(s). Published by the Royal Society of Chemistry

Open Access Article. Published on 25 August 2023. Downloaded on 2/6/2026 1:27:51 PM. This article is licensed under a Creative Commons Attribution-NonCommercial 3.0 Unported Licence.

nanomaterials may meet the requirements for becoming a promising photocatalyst.[7,8] Spinel ferrites are ferrimagnetic semiconducting materials having two different kinds of sites *i.e.*, tetrahedral (A) and octahedral (B) co-ordinated sites. Superexchange magnetic interactions (A–O–B) *via* oxygen atoms between tetrahedral (A) and octahedral (B) sites are the origin of ferrimagnetism in spinel ferrites. These A–O–B exchange interactions are stronger than the A–O–A and B–O–B sublattice interactions. The magnetic moments of these two sublattices are exactly the opposite with respect to each other, therefore, the overall magnetic moment (μ_T) of the system can be obtained by performing an algebraic subtraction of magnetic moments of both sites, *i.e.*, $\mu_T = (\mu_B - \mu_A)$ where both μ_B and μ_A represent the magnetic moment of octahedral (B) and tetrahedral (A) sites.[12,13] In photocatalytic applications, the most important part is the recollection and reuse of photocatalysts. Because of the magnetic behaviour of ferrite nanoparticles, it is easier to separate them using a strong magnet.[14,15]

In the entire cubic spinel ferrite family, nanocrystalline Ni–Zn spinel ferrites are known for their soft ferrimagnetic and semiconducting nature, having a moderate Néel temperature. These magnetic nanomaterials also exhibit excellent chemical and thermal stability, opening the door to various technological applications. In nanosized Ni–Zn ferrites, all the Zn^{2+} ions prefer to capture tetrahedral voids; Ni^{2+} ions have a strong tendency to occupy octahedral voids and Fe^{3+} ions are distributed in both octahedral and tetrahedral sites.[16,17] When a bulk material is shrunk down into nanoscale dimensions, it exhibits different physical properties due to the increase of surface atoms compared to volume. The physical properties of nanoparticles are highly influenced by the size, shape, morphology, nature of dopants and synthesis methods, which enables effective ways of tuning these properties. There are numerous techniques available for preparing Ni–Zn ferrite nanoparticles. Among these preparation methods, we have used the wet chemical co-precipitation method because it provides superior regularity in both shape and size of ferrite nanoparticles. This method is also a low-cost and easier route for preparing ferrite nanoparticles.[18] Different calcination temperatures have been applied for varying the size of Ni–Zn ferrite nanoparticles and also for tuning the physical properties.[19] It should be emphasised that the size affects the physical properties of nanocrystalline spinel ferrites. One can adjust the physical characteristics of ferrite nanoparticles by varying their size. Several novel phenomena can be introduced including the exchange bias effect, superparamagnetism, and disorderliness in the surface spins by modulating the size of the ferrite nanoparticles.[19] These fine-tuned ferrite nanoparticles of different sizes can be utilized for better-controlled spintronics, memory storage, hyperthermia, and other device applications.[12,13]

In this study, we present a detailed study with appropriate scientific explanations on the role of size change in modifying and tuning the microstructural, optical and magnetic properties. The indirect optical band gap of the prepared magnetic nanoparticles has been tuned by varying their size. The superparamagnetic phenomenon has also been introduced to our samples by varying the mean size. Magnetic moments, coercive field and blocking temperature of the ferrite nanoparticles have also shown a strong dependence on size.

The size of the nanoparticles has also modified the surface properties and affects the nanomaterial's porosity that is easily visible in the photocatalytic activities and antioxidant properties of our synthesized samples. This work also aims to provide a deep understanding of size-dependent photocatalytic activities of Ni–Zn ferrite nanoparticles in reducing toxic dyes from wastewater. A pH-reliant investigation on catalytic photodegradation was also conducted for the prepared nanoferrites. The antioxidant properties of ferrite nanoparticles were explored suitably. A systematic investigation with possible scientific explanations is presented in this article. This work revealed a possible cost-effective approach for wastewater management as the synthesis of Ni–Zn ferrite nanoparticles *via* the co-precipitation method is simple and easy. It also requires less time and low cost to prepare the nanoparticles and the smallest sized ferrite nanoparticles are highly efficient in degrading toxic dyes.

Experimental details

Synthesis of ferrite nanoparticles

Zinc doped nickel ferrite nanoparticles with a chemical composition of $Zn_{0.3}Ni_{0.7}Fe_2O_4$ were prepared by the conventional wet chemical co-precipitation method.[12,13] The prepared samples were marked as ZNF-1, ZNF-2 and ZNF-3 based on increasing average size. The detailed synthesis method can be found in the ESI.†

Photodegradation of methylene blue

Under xenon light, a succession of Ni–Zn ferrite nanoparticles was utilized for Methylene Blue (MB) degradation. All the experiments reported in this article were carried out using distilled water as a solvent. The temperature of the reaction during the experiment was found to be in between 25 °C and 30 °C. In 100 mL MB solution having a concentration of 30 mg L^{-1}, 0.1 g of ferrite nanoparticle sample was mixed and the mixture was then kept under the illumination of xenon light. A perfect adsorption–desorption equilibrium between the prepared samples and the MB solution was observed after the solution had previously been stirred in the dark for 12 hours at room temperature. Further, 200 μL of 50% hydrogen peroxide (H_2O_2) was added to the mixture to develop a Fenton-type system. The H_2O_2 was added to enhance the photodegradation, which resulted in the rapid generation of oxidation contaminants.[20] Further, 2–4 mL of the MB solution was taken out several times to observe degradation at a specified time interval.[3,21] UV-vis spectroscopy was used to monitor the photocatalytic degradation of MB dye in the solution. The degradation efficiency (in %) of the MB dye was determined using the following equation[4,22,23]

$$D(\%) = \left(1 - \frac{C_t}{C_o}\right) \times 100\% = \left(1 - \frac{A_t}{A_o}\right) \times 100\% \quad (1)$$

Open Access Article. Published on 25 August 2023. Downloaded on 2/6/2026 1:27:51 PM. This article is licensed under a Creative Commons Attribution-NonCommercial 3.0 Unported Licence.

where C_o corresponds to the initial concentration of MB dye and C_t is the dye concentration after a particular time interval. Similarly, A_o and A_t are the initial and final absorbance of the MB solution which was calculated at the peak point of the highest absorbance ($\lambda = 665$ nm) of MB dye.

Measurement of antioxidant activity

The antioxidant activity of Ni–Zn ferrite nanoparticles of different sizes (ZNF-1, ZNF-2 and ZNF-3) was evaluated by a 2,2-diphenyl-1-picrylhydrazyl (DPPH) scavenging assay described by Das *et al.*[24,25] with necessary modifications. In a typical process, 10 mL of 0.1 mM DPPH (in methanol) reagent was taken in a centrifuge tube and 4 mg of ferrite nanoparticles were mixed using a vortex and kept in a dark place to facilitate the surface reaction between the nanoparticles and DPPH reagent for 30 min. Ferrite nanoparticles scavenge the free radicals, which are generated by DPPH. In solution, DPPH radicals have a deep violet hue that gradually starts to fade and eventually turns pale yellow. This characteristic enables visual reaction monitoring and a change in the percentage of absorption at 517 nm can be used to track the concentration of radicals. The reaction mixture was vortexed at room temperature to increase the rate of the reaction. At various times, the supernatant containing DPPH was collected. The time-dependent DPPH scavenging method was studied at an interval of 30, 60, 90, 120 and 150 min for ZNF-1, ZNF-2 and ZNF-3 samples. The absorbance of the optically transparent supernatant was observed at 517 nm using a UV-vis spectrophotometer by taking methanol as a reference. The percentage of DPPH scavenging activity is calculated using the stated equation[26]

$$\text{DPPH scavenging activity}(\%) = \left[1 - \frac{A_s}{A_c}\right] \times 100\% \qquad (2)$$

where A_c and A_s are the intensity of the peak at 517 nm for the control (DPPH in methanol) and supernatant of ZNF samples respectively.

Characterization

The identification of the developed single spinel-phase of all the ZNF samples together with morphology, microstructural, magnetic and optical properties was investigated carefully using X-ray diffractograms, high-resolution transmission electron microscopy (HRTEM), FESEM, FTIR spectroscopy, vibrating sample magnetometer (VSM) and UV-vis spectroscopy. Details of the characterization techniques used are found in the ESI.†

Results and discussion

X-ray diffractogram studies

Fig. 1(A) shows the room temperature X-ray diffraction patterns of all three $Zn_{0.3}Ni_{0.7}Fe_2O_4$ ferrite samples annealed at different temperatures. Attentive analysis of diffraction patterns validated the existence of a single cubic spinel crystallographic phase structure having space group *Fd*-3*m*. All the diffraction profiles exhibited characteristic peaks of spinel cubic structure with the maximum intensity (311) peak near 35.51°. The absence of any other peaks apart from the characteristic peaks in the diffraction patterns specified the non-existence of foreign elements.[13,19] All the obtained peaks in the diffractograms were found to have an excellent match with JCPDS card number 10-325. Rietveld refinement of all the diffractograms was performed using General Structure Analysis System (GSAS) software with EXPUGI as an interface. The pseudo-Voigt function (superposition of Lorentzian and Gaussian functions) along with Finger–Cox–Jephcoat asymmetry for correcting axial divergence was used to fit all the profile peaks. All the microstructural parameters, unit cell parameters, refinement factors such as goodness of fit (χ^2) and reliability factors (R_P and R_{WP}) are displayed in Table S1 in the ESI.† The obtained values of χ^2 of nearly one for all the samples together with refinement factors within the acceptable limit (less than 5%) signified the strong agreement between the theoretical and recorded data of XRD patterns. A clear broadening in diffraction profiles was observed and it was reduced gradually for the samples annealed at high temperatures.[27,28] The lack of long-range crystalline arrangements of atoms in tiny crystallites and developed microstrain inside the crystallites were mainly responsible for the observed broadening in diffraction peaks. In addition, broadening due to the instrumental effect also contributed effectively to the overall broadening of XRD peaks. The instrumental broadening effect was eliminated by taking a diffraction

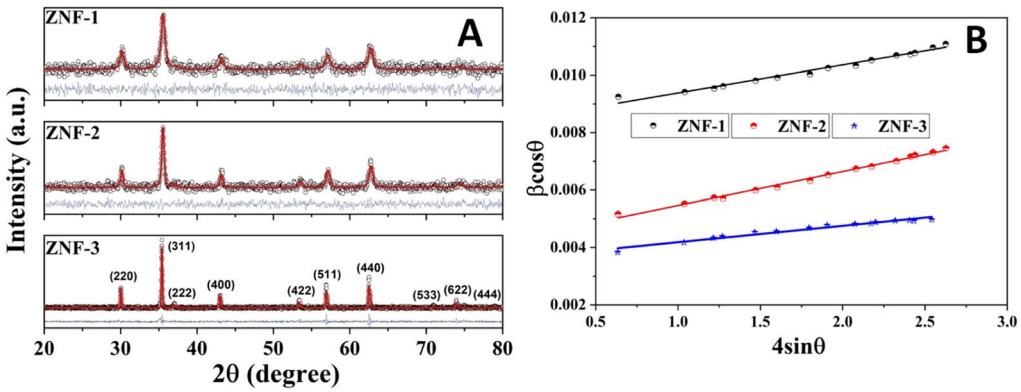

Fig. 1 (A) Rietveld refinement of the XRD patterns of all the ferrite samples and (B) Williamson–Hall (W–H) plots of all the samples.

© 2023 The Author(s). Published by the Royal Society of Chemistry

Open Access Article. Published on 25 August 2023. Downloaded on 2/6/2026 1:27:51 PM. This article is licensed under a Creative Commons Attribution-NonCommercial 3.0 Unported Licence.

pattern of a bulk sample having the same compositions under identical conditions. After terminating the instrumental broadening effect, the overall measured line width β (FWHM) of a peak is merely the algebraic sum of broadening effects due to nanocrystallite size (β_{size}) and microstrain (β_{strain}) and can be written as[12,18]

$$\beta = (\beta_{size} + \beta_{strain}) = \frac{K\lambda}{D\cos\theta} + 4\varepsilon\tan\theta \quad (3)$$

where K is known as a geometric factor (it attains a value of 0.9 for spherical shaped nanoparticles), λ is the wavelength (1.5406 Å) of the Cu K_α X-ray line, ε specifies the microstrain present inside the nanocrystals, D is the average crystallite size and θ represents Bragg's angle. After reorganization, eqn (3) gains the form as stated[18,29]

$$\beta\cos\theta = \varepsilon(4\sin\theta) + \frac{0.9\lambda}{D} \quad (4)$$

Separation of these two broadenings due to nanosize and microstrain effects in overall peak broadening was performed successfully by plotting a graph (straight line) of $\beta\cos\theta$ as a function of $4\sin\theta$. This graph is known as the Williamson–Hall (W–H) plot which is depicted in Fig. 1(B).

In W–H plots, the slope of the straight line provides the value of microstrain (ε) present in nanocrystals and the intercept on the $\beta\cos\theta$ axis is simply equal to $0.9\lambda/D$. The calculated values of mean crystallite size were 16.4 nm (ZNF-1), 21.1 nm (ZNF-2) and 38.3 nm (ZNF-3) respectively as per increasing sintering temperatures.[30] The developed microstrain in nanocrystals was tensile in behavior for all the samples because the slopes were positive as shown in Table S1.† In inverse spinel cubic $NiFe_2O_4$ crystal structure where all the Fe^{3+} ions are distributed equally in both tetrahedral and octahedral voids, Zn^{2+} ions always exhibit a strong tendency to occupy tetrahedral sites. Due to the smaller size of Zn^{2+} (0.60 Å) ions compared to Fe^{3+} (0.645 Å) ions and the mismatch in valency, oxygen vacancies are produced, significantly affecting the developed microstrain in nanocrystals. It is noted that both the mean crystallite size (D) and lattice parameter (a) increased with increasing the annealing temperature of nanocrystalline Ni–Zn ferrites.[30] This minute enhancement in lattice parameter is attributed to the better crystalline nature of the prepared samples with increasing the annealing temperature. Spinel Ni–Zn ferrite samples gained good crystallinity and comparatively large crystalline coherence length with the increment of annealing temperature.

The oxygen positional parameter (u) normally provides the relative movement of O^{2-} ions in both tetrahedral and octahedral sublattices for the spinel structure.[31] As seen from Table S1,† no notable change in the estimated values of u was found for all the ferrite nanoparticles. It is known that the average size of tetrahedral voids is smaller with respect to octahedral voids so Zn^{2+} ions pushed O^{2-} ions during the adjustment in tetrahedral voids but due to the presence of oxygen vacancies, this effect may be compensated for, thereby there was no notable change in u. Generally, the obtained value of u is slightly larger than the ideal value (0.375) for spinel cubic crystal structure while considering the origin at the tetrahedral site. This is due to the fact of basic consideration where atoms are considered as hard spheres but behave as quantum systems having diffuse boundaries.[16] The hopping lengths of both tetrahedral (A) and octahedral (B) sites ($L_A = \sqrt{3}\frac{a}{4}$ and $L_B = \sqrt{2}\frac{a}{4}$) were observed to increase minutely for the samples that contained a higher mean size of nanoparticles. This is ascribed to the increase in the values of the lattice constant. Hopping lengths in spinel structures basically bear the information of magnetic interactions and charge transfer methods. A slight increment in hopping lengths implies that the demand of energy for an electron to jump from one site to another becomes comparatively higher.[19,31]

Analysis of HRTEM images

HRTEM images of all the as-synthesized ZNF-1, ZNF-2 and ZNF-3 samples are shown in Fig. 2(a)–(c), respectively. All the images exposed that the prepared nanoparticles were almost spherical in shape, homogeneous and showed an excellent match with mean crystallite sizes as obtained from W–H plots. Significant agglomeration in ferrite nanoparticles for all the samples was noticed. Observed aggregation among the magnetic nanoparticles is attributed to both the dipole–dipole interactions and van der Waals interactions.[12,13,16] ImageJ software was used to draw the histograms for estimating the average particle size of all the ferrite samples.[12] The obtained mean sizes of the nanoparticles were 19.2 ± 0.1 nm, 24.3 ± 0.1 nm and 42.7 ± 0.1 nm respectively for ZNF-1, ZNF-2 and ZNF-3 samples, and were observed to be close to the crystallite sizes.

The existence of concentric circular rings in the selective area electron diffraction (SAED) pattern of the ZNF-3 sample verified the high crystalline ordering and formation of the spinel cubic crystallographic phase. The identification of (111),

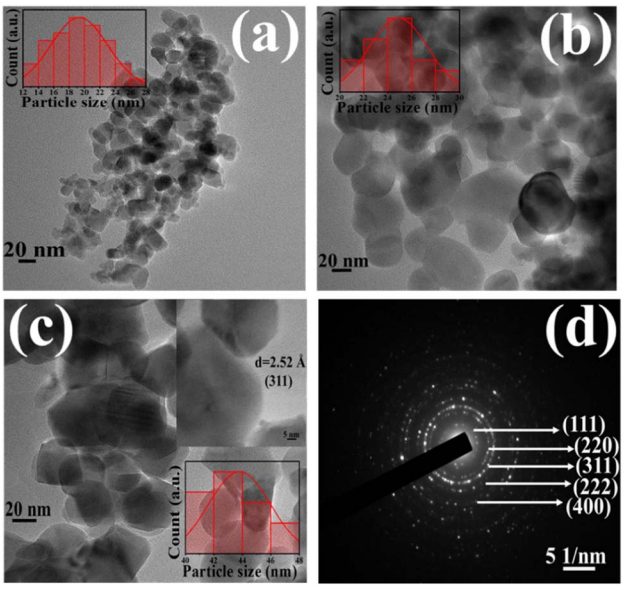

Fig. 2 (a–c) HRTEM micrographs of the ZNF-1, ZNF-2 and ZNF-3 samples and (d) SAED pattern of the ZNF-3 sample.

Open Access Article. Published on 25 August 2023. Downloaded on 2/6/2026 1:27:51 PM. This article is licensed under a Creative Commons Attribution-NonCommercial 3.0 Unported Licence.

(220), (311), (222) and (400) crystallographic planes was done in the SAED pattern from where electrons were diffracted and is shown in Fig. 2(d). A careful examination of the SAED pattern disclosed that all the concentric rings were not equi-spaced.[19,32,33] The first two rings were located close enough whereas the third ring was placed far apart and the identical formation was repeated. Such kind of configuration of concentric rings implied the presence of interpenetrating face-centred cubic (FCC) lattices in the spinel cubic crystal structure.[30] The inset of Fig. 2(c) depicts the highly crystalline nature of the ZNF-3 sample and a set of parallel (311) planes with an interplanar distance of 2.52 Å was marked in that same image.[19]

UV-vis spectra studies

Optical properties especially the indirect band gap of Ni–Zn ferrite nanoparticles having different particle sizes were examined by recording absorption spectra at room temperature within the range of 200 nm to 800 nm. It is stated that the nickel ferrite in bulk form exhibits an indirect optical band gap of around 1.65 eV together with two different allowed direct band gaps at relatively higher energy bands.[34,35] The optical band gap energy of ferrite nanoparticles is commonly determined by using the Tauc relation, which is stated below[36]

$$\alpha(\nu)\cdot h\nu \approx C(h\nu - E_o)^n \quad (5)$$

where 'C' is an arbitrary constant, 'E_o' denotes the optical band gap of ferrite nanoparticles, 'α' represents the absorption coefficient and 'n' signifies an arbitrary index. The index 'n' possesses a definite value *i.e.*, 2 for an indirect optical transition. For evaluating the indirect optical band gap of Ni–Zn ferrite nanoparticles, a plot of $(\alpha h\nu)^{0.5}$ with respect to photon energy ($h\nu$) was drawn which is shown in Fig. S1 in the ESI.† Values of absorption coefficient (α) for all the prepared samples were evaluated from the absorbance (A) data collected at 300 K obeying these two primary relationships[16,36]

$$I = I_o e^{-\alpha d} \text{ and } A = \log_{10}\left(\frac{I_o}{I}\right) \quad (6)$$

Therefore $\alpha = 2.303\left(\frac{A}{d}\right)$, where '$d$' represents the width of the cuvette used to keep the sample. The evaluated values of the indirect optical band gaps were 1.81 eV, 1.76 eV and 1.73 eV for ZNF-1, ZNF-2 and ZNF-3 ferrite samples. A red shift in the indirect band gap with increasing average particle size was clearly observed. It is a common feature of the nanoscale domain and can be ascribed to the nanosize effect of the prepared ferrite samples. Due to the reduction in the number of atoms inside a particle when it attains nanosize, the overlapping of various electronic orbitals decreases as compared to bulk samples. As a result, energy bands become narrower and more discrete, which leads to an increment in the energy band gap.[30,37] All the synthesized Ni–Zn ferrite nanoparticles clearly exhibited an opaque nature in the red and near IR region of the EM spectrum, therefore, these samples would be promising materials for various optical applications.

Magnetic properties analysis

Temperature-dependent magnetization (M–T) curves of all the Ni–Zn ferrite samples were recorded under a dc magnetic field (500 Oe) in both field cooled (FC) and zero field cooled (ZFC) protocols. All the M–T data were registered during the heating cycle and are shown in Fig. 3. The temperature at which the ZFC curve exhibits a maximum is known as blocking temperature (T_B). At blocking temperature, the thermal energy ($k_B T_B$) of the

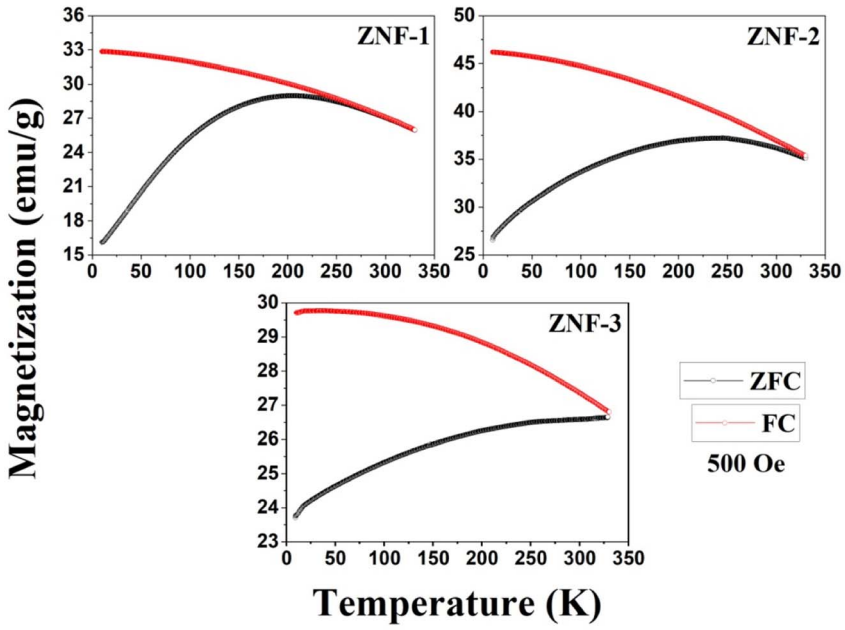

Fig. 3 M–T plots of all the ferrite samples.

© 2023 The Author(s). Published by the Royal Society of Chemistry

Open Access Article. Published on 25 August 2023. Downloaded on 2/6/2026 1:27:51 PM. This article is licensed under a Creative Commons Attribution-NonCommercial 3.0 Unported Licence.

system is equal to the effective magnetic energy barrier. A coherent flipping of spins usually occurs above T_B whereas spins are blocked below T_B as the need for energy to overcome the energy barrier is not fulfilled.[38] A decrement in overall magnetization was also detected below T_B due to the blocking of spin moment of ferrite nanoparticles along the easy axis. Ferrite nanoparticles lost their ferrimagnetic behavior above blocking temperature and also exhibited insignificant coercivity and remanence. This magnetic ground state with insignificant coercivity and remanence above T_B is characterized as a superparamagnetic (SPM) state. As our studied system consists of a large number of magnetic nanoparticles, the obtained blocking temperature is an average value. The blocking temperature (T_B) of a magnetic system containing nanoparticles is strongly controlled by three primary parameters, *i.e.*, average volume (V_S) of magnetic nanoparticles, effective anisotropy constant (K) and measurement time of the instrument.[16,19,38]

The blocking temperature of a magnetic system having a large number of nanoparticles can be expressed as[38]

$$T_B = \frac{KV_S}{25k_B} \quad (7)$$

where K denotes the effective anisotropy constant. The blocking temperature was noted to increase with the increasing mean size of Ni–Zn ferrite nanoparticles. With the increase of mean size, the requirement of thermal energy (k_BT) increases to beat the magnetic energy barrier (KV_s) of the system, therefore, T_B also increases. As observed in Fig. 3, the ZNF-1 and ZNF-2 samples revealed average blocking temperatures of 203 K and 251 K respectively whereas the ZNF-3 sample showed T_B above room temperature. Magnetic hysteresis responses collected at 300 K also obeyed the results estimated from M–T measurements. An attentive observation revealed that the ZFC and FC curves in M–T measurements began to split at a specified temperature which is characterized as thermo-magnetic irreversible temperature (T_{irr}). Information on the deblocking temperature of spin moments for the largest nanoparticles present in the sample is given by T_{irr}.[38] The obtained values of T_{irr} for ZNF-1 and ZNF-2 samples are 249 K and 329 K respectively whereas for the ZNF-3 sample, it is above 330 K. The noted increment in the values of T_{irr} is attributed to the enhancement in the mean size of ferrite nanoparticles. Separation between T_{irr} and T_B bears a general picture of the width of magnetic energy barrier and also the size distribution of Ni–Zn ferrite nanoparticles.[38,39] To have a narrow anisotropy energy barrier and a narrow particle size distribution for a magnetic system, the difference between T_{irr} and T_B must be minimal. This ($T_{irr} - T_B$) difference became minimal for the ZNF-1 nanocrystalline ferrite sample. The observed irreversibility in Fig. 3 between ZFC and FC protocols in the low temperature (nearly 10 K) zone can be understood by the stated empirical relation[40]

$$M_{ZFC} = M_{FC}\frac{H_A}{2H_C}(H_A < 2H_C) \quad (8)$$

where H_A is the applied static magnetic field (500 Oe) and H_C signifies the coercivity of that system. Irreversibility between ZFC and FC curves may disappear when the applied static magnetic field is much greater than the coercive field of the magnetic system. The observed separation between ZFC and FC curves for all the ferrite samples especially at low temperatures is due to the freezing of spins along their easy direction below T_B.[38,40]

Fig. 4(A) shows the magnetic hysteresis loops of all the Ni–Zn ferrite samples registered at 5 K under the application of a ±50 kOe magnetic field. All the ferrite nanoparticles displayed ferrimagnetic behavior with significant coercive field and saturation magnetization at 5 K.[12] The estimated values of saturation magnetization (M_S), coercive field (H_C), remanence ratio (M_r/M_s), magnetic moment (μ_T) and effective anisotropy constant (K) for all the ferrite samples are listed in Table 1. The saturation magnetization of all the ferrite samples increased with increasing mean particle size while coercivity reduced gradually at 5 K as observed in Table 1. With the increase of average particle size, nanosized systems become more crystalline and also attain comparatively long-range ordering of atoms, thereby these systems try to gain the bulk value of M_S which may result in a gradual increment of saturation magnetization.[12,13]

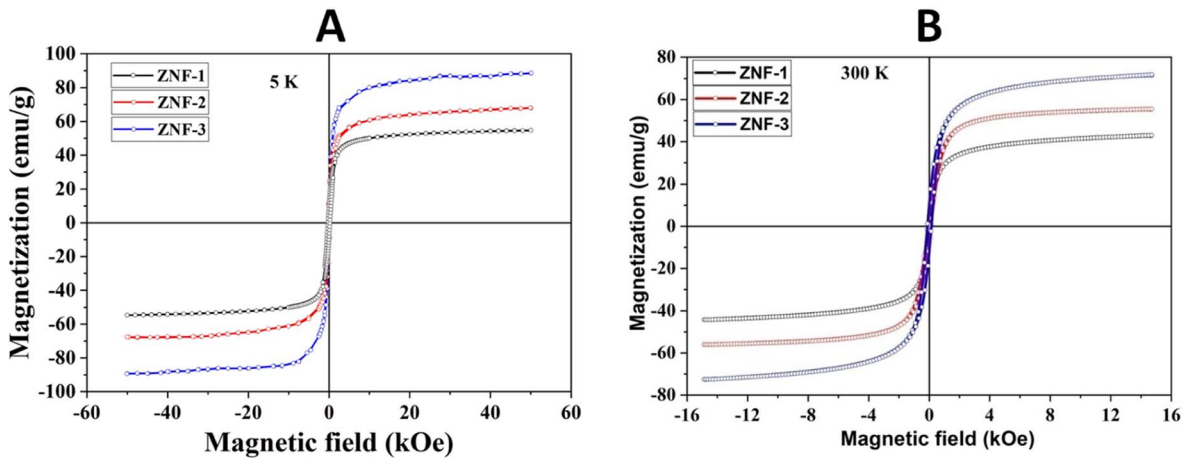

Fig. 4 (A) Hysteresis loops of all the samples registered at 5 K and (B) hysteresis loops of all the samples collected at 300 K.

Open Access Article. Published on 25 August 2023. Downloaded on 2/6/2026 1:27:51 PM. This article is licensed under a Creative Commons Attribution-NonCommercial 3.0 Unported Licence.

Table 1 Unit cell parameters and Rietveld refinement factors of all the Ni–Zn ferrite samples

	Magnetic properties									
	5 K					300 K				
Sample id	M_S (emu per g)	H_C (Oe)	$\frac{M_r}{M_s}$	$K\left(\frac{\text{emu kOe}}{\text{g}}\right)$	μ_T (μ_B)	M_S (emu per g)	H_c (Oe)	$\frac{M_r}{M_s}$	$K\left(\frac{\text{emu kOe}}{\text{g}}\right)$	μ_T (μ_B)
ZNF-1	54.3	324	0.17	17.952	2.29	42.7	19	0.03	0.828	1.80
ZNF-2	67.5	255	0.15	17.563	2.86	55.2	93	0.10	5.238	2.33
ZNF-3	88.9	178	0.13	16.147	3.76	71.5	119	0.08	8.682	3.02

With the decrease in size, several surface effects such as the existence of disordered surface spins, canted spins and magnetically dead layers at the surface become more prominent for magnetic nanoparticles. Also due to the high surface-to-volume ratio, the atoms present at the surface of the nanoparticles take active participation in deciding the overall properties of the system in comparison to the bulk. The observed reduction in saturation magnetization with decreasing particle size is also attributed to several surface effects of ferrite nanoparticles. It is accepted that the saturation magnetization of ferrite nanoparticles intensively depends upon both the mean particle size (D) and thickness (t) of the dead spin layer that exists at the surface. Regarding magnetic nanoparticles, the saturation magnetization follows the stated relation[41]

$$M_S = M_O\left(1 - \frac{6t}{D}\right) \quad (9)$$

where M_O specifies the saturation magnetization of a bulk sample. With the increase of particle size, the saturation magnetization increases towards the bulk value.

A systematic reduction in coercivity was also observed for the samples containing comparatively larger-sized nanoparticles. The increment of disordered surface spins, canted spins and various surface effects with a decrease in mean size also enhances the effective anisotropy constant (K) of the magnetic nanoparticles, therefore more energy is needed for the magnetic reversal to happen, and coercivity increases.[9] The decrement in coercivity at 5 K for the samples containing comparatively larger sized nanoparticles also heavily affects both the saturation magnetization and effective anisotropy constant (K) of the ferrite system which can be understood by the stated expression[42]

$$H_C = \frac{0.98\ \text{K}}{M_S} \quad (10)$$

Values of the effective anisotropy constant (K) of all the ferrite samples were calculated and tabulated in Table 1. A notable reduction in the values of K was found with the increase in the size of the synthesized ferrite nanoparticles.

The applied magnetic field (±15 kOe) dependent magnetization (M–H) of all the ferrite samples registered at room temperature is displayed in Fig. 4(B). The estimated values of various magnetic parameters from hysteresis loops such as M_S, H_C and K of entire samples are collected in Table 1. The ZNF-1 sample containing the smallest-sized nanoparticles exhibited insignificant remanence and coercive field; hence this ferrite sample is considered to be superparamagnetic at 300 K.[16,19] The coercive field of all the ferrite samples was noted to increase with the increase of particle size at 300 K. In case of single domain ferrite nanoparticles, the coercive field (H_C) varies with mean particle size (D) as stated by the empirical relation[43]

$$H_C = \alpha - \frac{\beta}{D^{\frac{3}{2}}} \quad (11)$$

where both 'α' and 'β' are arbitrary constants. Therefore, coercivity also increases with the increase of average particle size below a critical size. A systematic enhancement in M_S was noticed for larger size ferrite nanoparticles at 300 K. This is due to the weakening of several surface effects, thereby magnetic systems attempt to obtain the M_S of bulk ferrites. Based on Néel's model, spinel ferrites' total magnetic moment (μ_T) is the algebraic subtraction of the net magnetic moment of entire octahedral and tetrahedral sublattices. The effective total magnetic moment (in μ_B) per formula unit is obtained using the following relation[44]

$$\mu_T = \frac{M_S M}{5585} \quad (12)$$

where M corresponds to the molecular weight (per formula unit) of Ni–Zn ferrites. Values of the magnetic moment were found to increase at both 5 K and room temperature for all the ferrite samples due to an increase in saturation magnetization (M_S). The existence of microstrain inside the nanocrystals also favours the non-collinear grouping of surface spins that highly affects the magnetic moment and saturation magnetization.[12] The obtained values of remanence ratio (M_r/M_S) normally reduced with the decrease of mean size for Ni–Zn nanoferrites at 300 K also assist the SPM behaviour of ferrite nanoparticles.

Zeta potential studies

Both the surface charge and dispersion stability of Ni–Zn ferrite nanoparticles of different sizes in an aqueous solution were determined by the zeta potential. The surface charge of nanoparticles plays a crucial role in attracting the aqueous contaminants on the surface and enhancing the photocatalyst activity. Ultimately, the highly dispersed photocatalyst in an aqueous solution shows greater photodegradation activity. With an increase in charge density on the surface of nanoparticles, electrostatic repulsion increases between particles, thereby

 © 2023 The Author(s). Published by the Royal Society of Chemistry

Open Access Article. Published on 25 August 2023. Downloaded on 2/6/2026 1:27:51 PM. This article is licensed under a Creative Commons Attribution-NonCommercial 3.0 Unported Licence.

more stable suspensions can be obtained. It is known that the zeta potential of a photocatalyst may affect the adsorption of targeted contaminants in a positive or negative way. The zeta potential stimulates the adsorption of contaminants positively if the contaminants are oppositely charged with respect to the photocatalyst surface.[15,45,46] Fig. S2(a)–(c) in the ESI† show the zeta potential of all the synthesized Ni–Zn ferrite samples. The evaluated values of zeta potential are 26.2 mV, 15.9 mV and −14.8 mV for ZNF-1, ZNF-2 and ZNF-3 samples respectively. The ZNF-1 sample containing the smallest sized magnetic nanoparticles exhibited comparatively higher zeta potential and values of zeta potential were found to reduce with increasing mean size of particles for other samples. The increase in zeta potential with the reduction of average particle size also confirmed the better stability of nanoparticles in an aqueous solution which may result in excellent photodegradation activity.[47,48]

FTIR spectra analysis

The existence of several chemical bonds in a compound and the formation of functional groups can be identified by FTIR spectroscopy. It can also be used as a fingerprint technique for pointing out different compounds. Fig. S3 in the ESI† shows the room temperature FTIR spectra of all the Ni–Zn ferrite samples. It is reported that the spinel cubic structure exhibits two vibrations of metal–oxygen (M–O) bonds in the range of 350 cm^{-1} to 600 cm^{-1}. The presence of these two vibrational peaks also verifies the formation of the spinel cubic crystallographic phase.[3,4] The first characteristic absorption peak for all the samples was detected in the domain of 548.5 cm^{-1} to 555.6 cm^{-1} which specifies the stretching of metal–oxygen (Fe–O) bonds at tetrahedral (A) sites. The second characteristic absorption peak was noticed near 400 cm^{-1} for all the ferrite samples which arises due to the stretching of M–O (M = Ni, Zn) bonds at octahedral (B) sites. The first characteristic peak was found to shift towards a higher wavenumber with increasing mean size of ferrite nanoparticles.[3,4,46] In general, the characteristic vibration frequency of spinel ferrites is highly influenced by the three primary factors *i.e.*, reduced mass, the spring constant of the bond and the length of the metal–oxygen bond.

Analysis of N_2 adsorption/desorption isotherms (BET study)

In the photodegradation of dyes, the surface of the photocatalyst and several parameters such as porous structure, specific surface area, pore size and total pore volumes associated with it provide a significant impact. All three samples were examined at 250 °C in the presence of a N_2 gas flow for 17 hours. The nitrogen adsorption–desorption isotherms of all three ferrite samples are displayed in Fig. 5(a)–(c). Both the specific surface area and pore radius were determined using a Brunauer–Emmett–Teller (BET) surface analyzer. As noticed in the isotherms, the adsorption increased slowly in the low pressure region and then enhanced rapidly when P/P_0 became more than 0.80. Isotherms of all three samples are matched with a typical type IV adsorption isotherm which specifies the presence of

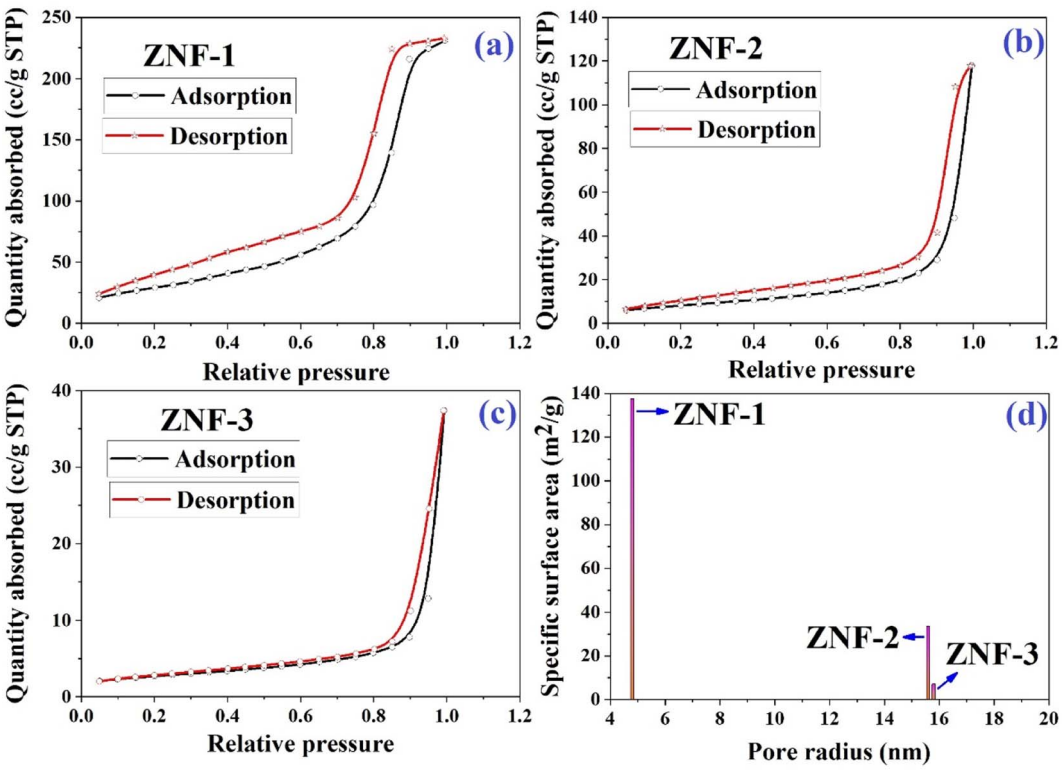

Fig. 5 (a–c) Nitrogen gas adsorption–desorption isotherms of ZNF-1, ZNF-2 and ZNF-3 ferrite samples and (d) plot of specific surface area as a function of pore radius.

Open Access Article. Published on 25 August 2023. Downloaded on 2/6/2026 1:27:51 PM. This article is licensed under a Creative Commons Attribution-NonCommercial 3.0 Unported Licence.

a mesoporous structure.[2,3,48] It is accepted that with the decrease in particle size, the surface area of a catalyst increases significantly which improves the dispersion in an aqueous solution and boosts the photocatalytic activity.

The acquired specific surface areas for ZNF-1, ZNF-2 and ZNF-3 ferrite samples are 137.63 $m^2\ g^{-1}$, 33.78 $m^2\ g^{-1}$ and 7.11 $m^2\ g^{-1}$ with corresponding pore radii of 4.785 nm, 15.612 nm and 15.799 nm respectively. The sample containing ferrite nanoparticles of smallest mean size *i.e.*, ZNF-1 is more porous compared to the other samples. It is observed in our case with the increase of size that the porosity of the prepared samples decreases. A histogram of the specific surface area of all the samples as a function of pore radius is drawn and shown in Fig. 5(d). The higher specific surface area of ZNF-1 nanoparticles enables more contact sites for photocatalytic reactions and as a result the photodegradation of dye becomes faster compared to other samples.[3,14]

Study of photocatalytic effects

Fig. 6(a)–(c) show the photodegradation of MB using Ni–Zn ferrite nanocatalysts (ZNF-1, ZNF-2 and ZNF-3) under the illumination of a xenon lamp. A decrease in the absorbance of MB was clearly noticed with increasing the duration of reaction time under radiation. Samples were collected several times in half hour intervals and the absorbance of MB was recorded. All the ferrite nanocatalysts having different sizes exhibited excellent photocatalytic activity in degrading MB dye.[49,50] Among all the prepared ferrite samples, the ZNF-1 sample containing smallest sized nanoparticles showed relatively superior photocatalytic activity.

It was observed that the ZNF-1 nanocatalyst degraded 93.8% of MB dye in 3 hours. However, ZNF-2 and ZNF-3 samples were capable of degrading 75.7% and 56.5% respectively in 3 hours. The degradation efficiency (in percentage) of all the ferrite nanocatalysts is depicted in Fig. 7. A decrement in degradation efficiency was found with increasing mean size. This is mainly due to the reduction in specific surface area, surface charge density and zeta potential. It is clearly understood that the degradation efficiency of our spinel Ni–Zn ferrite nanocatalysts strongly depends on the mean size of nanoparticles.[20] It is also noted that in the absence of ferrite nanocatalysts, there was no notable photon-mediated reduction of MB and change in color observed which implies that the photodegradation of MB was not actively triggered by H_2O_2 only.[3,4]

Without nanocatalysts, H_2O_2 alone was able to reduce only 15.41% of MB in 3 h under irradiation as shown in Fig. S4(a) (ESI†) and without any catalyst and H_2O_2, no significant change in MB degradation was noticed (Fig. S4(b), ESI†). As another important factor, the rate constant of the photodegradation reaction was also calculated for each sample. Kinetics of photodegradation for MB dye using ferrite nanocatalysts were examined by following 1st order and 2nd order rate equations[4,22,23]

$$\ln\left(\frac{C_o}{C_t}\right) = k_1 t \tag{13}$$

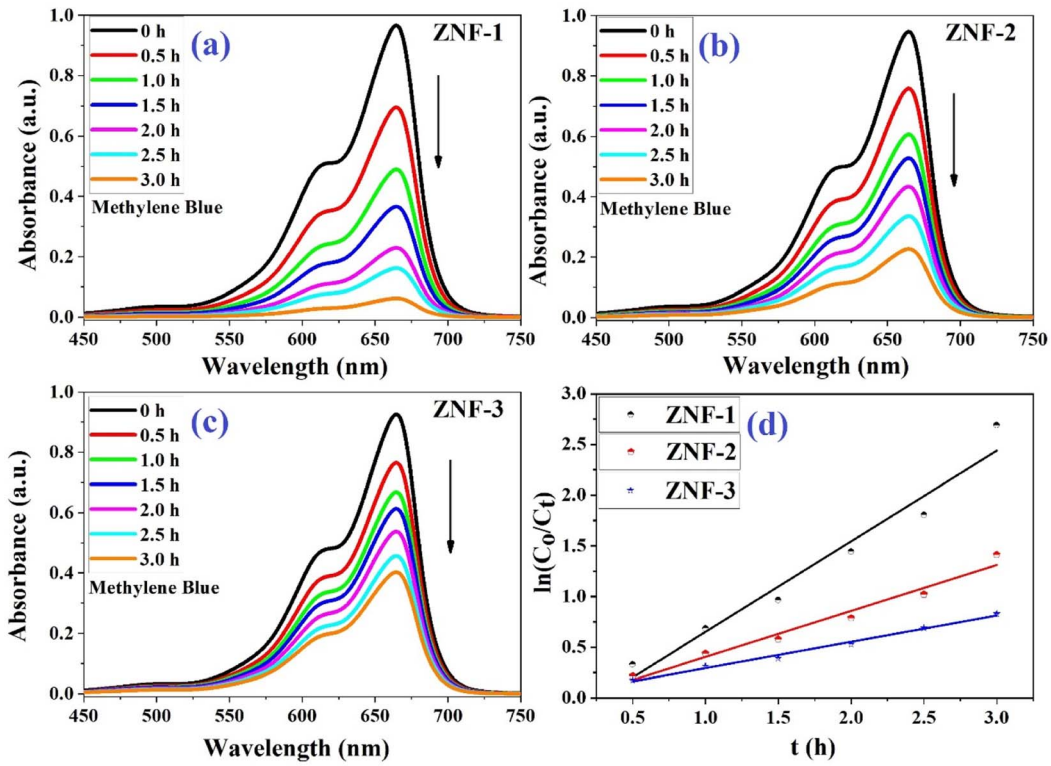

Fig. 6 (a–c) Photodegradation of MB dye using ZNF-1, ZNF-2 and ZNF-3 ferrite nanocatalysts and (d) plot of 1st order kinetics reaction rate equation.

© 2023 The Author(s). Published by the Royal Society of Chemistry

Open Access Article. Published on 25 August 2023. Downloaded on 2/6/2026 1:27:51 PM.
This article is licensed under a Creative Commons Attribution-NonCommercial 3.0 Unported Licence.

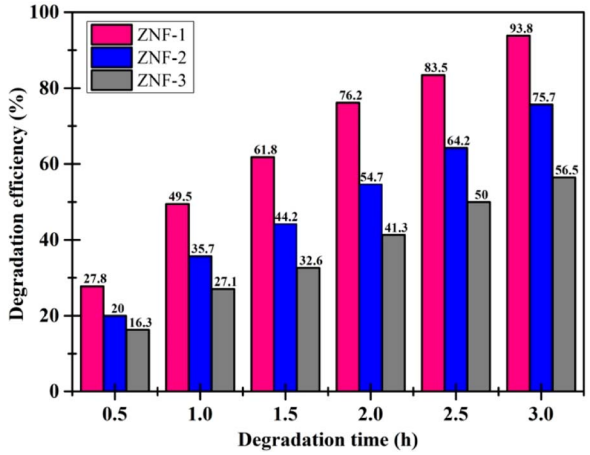

Fig. 7 Degradation efficiency of MB dye using ferrite nanoparticles.

$$\left(\frac{1}{C_t}\right) - \left(\frac{1}{C_o}\right) = k_2 t \quad (14)$$

where C_o and C_t are the initial and final concentration of MB dye, t denotes the exposure time of xenon light, k_1 signifies the 1st order reaction rate kinetics and k_2 represents the 2nd order reaction rate kinetics.[1,2] To understand the reaction kinetics, these two rate equations were plotted for each sample with respect to time and straight-line curves were obtained. Both Fig. 6(d) and S5 in the ESI† show the kinetics plots of the photodegradation reactions. The regression correlation coefficient (R^2) of the kinetics plots of each sample helps to identify the order of reaction and the slope of the straight line provides the rate constant. The obtained values of R^2 for both orders of kinetics obeying eqn (13) and (14) are listed in Table S2 in the ESI.† As seen from Table S2,† it is understood that the values of R^2 for first-order kinetics are greater than those of second-order kinetics for each nanocatalyst indicating that the photodegradation of MB dye obeys the first-order rate kinetics. The estimated values of rate constants for ZNF-1, ZNF-2 and ZNF-3 ferrite samples were 0.894 h^{-1}, 0.453 h^{-1} and 0.256 h^{-1} respectively. It is found that the smallest sized ZNF-1 nanocatalyst exhibited the highest value of rate constant. A comparative study on catalytic activities of recently reported spinel nanoferrites with our prepared magnetic nanocatalysts was carried out and is listed in Table 2.

Analysis of pH effect in degradation

In order to understand the impact of pH on photocatalyst degradation efficiency (PCD), the photocatalytic degradations were performed at different pH levels ranging from 3 to 9 for MB dye solution having a fixed MB concentration (3 mg per 100 mL) and catalyst loading (100 mg per 100 mL). For preparing solutions having the pH values, we used HCl and NaOH. The pH dependent photocatalytic activity of ZNF-1 ferrite nanocatalysts was recorded for 2 h and is depicted in Fig. S6 in the ESI.† As noticed from Fig. 8(A), the degradation efficiency decreased to 96.9%, 86.4%, 76.1% and 66.8% when the pH of the solution was increased to 3, 5, 7, and 9 respectively.

A systematic reduction in degradation efficiency was noted for higher pH solutions. It is clearly seen that MB degradation strongly relies upon the pH of the solution. Under xenon irradiation for 120 minutes, the maximum 96.9% PCD efficiency was observed at pH 3.[54] Therefore, the pH 3 solution was determined to be the ideal solution in this investigation since it required the least amount of time to degrade MB dye. The adsorption and degradation of MB dye depend on both the catalyst's surface charge and the solution's pH.[55] The observed maximum PCD efficiency at pH 3 is due to the electrostatic attraction between the positively charged surface of the nanocatalyst and anionic dye (MB). Nevertheless, when the pH level exceeds 7, the ZNF-1 nanocatalyst surface becomes negatively charged which causes electrostatic repulsion between the MB and catalyst and slowed down PCD efficiency.[5,56,57] In the pH 3 solution, the ZNF-1 photocatalyst displayed fast degradation with the highest value of 1st order rate constant due to the strong electrostatic attraction between the dye and nanocatalyst.[56] The rate constant gradually decreased for the samples having large sized nanoparticles as depicted in Fig. S7 in the ESI.†

Effects of surface area and particle size on the degradation of dye

Nanomaterials having high specific surface areas are more efficient in degrading dye for photocatalytic activity. As the

Table 2 Comparison of photocatalytic activities

Sl. no.	Catalysts	Method of synthesis	Rate constant (k) (min^{-1})	Ref.
1	Zinc ferrite NPs	Green synthesis	0.0087	2
2	Ni–Zn ferrite NPs	Combustion method	0.0238	5
3	Nickel ferrite NPs	Sol–gel technique	0.0018	51
4	Ni–Zn ferrite NPs	Sol–gel technique	0.0027	3
5	Zinc ferrite	Hydrothermal method	0.0011	1
6	Ni–Zn ferrite	Combustion method	0.0262	52
7	Mg–Co–Zn ferrite NPs	Citrate precursor method	0.0633	53
8	ZNF-1	Co-precipitation method	0.0150	This work
9	ZNF-2	Co-precipitation method	0.0076	This work
10	ZNF-3	Co-precipitation method	0.0043	This work

© 2023 The Author(s). Published by the Royal Society of Chemistry

Open Access Article. Published on 25 August 2023. Downloaded on 2/6/2026 1:27:51 PM.
This article is licensed under a Creative Commons Attribution-NonCommercial 3.0 Unported Licence.

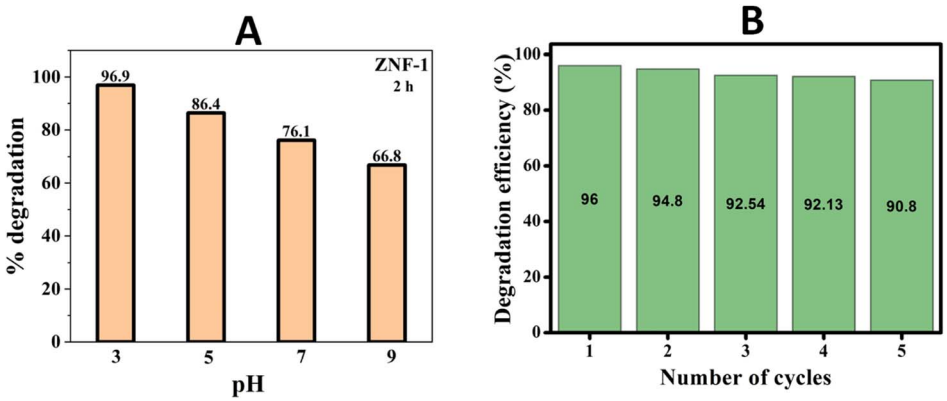

Fig. 8 (A) Percentage degradation of MB dye at different pH by the ZNF-1 nanocatalyst and (B) reusability histogram of the ZNF-1 photocatalyst.

particle size decreases, the surface area of the synthesized nanoparticles increases, and the electron–hole recombination rate also increases, which facilitates good dispersion of ferrite nanoparticles in the solution. A solution of well-dispersed catalysts improves the photon absorbance leading to increased catalytic activity. From BET measurements, the highest specific surface area was measured for the sample consisting of the smallest particle size (ZNF-1).[5] This result indicates that the increment in the surface area supports the enhancement of active sites in the sample. It is clearly understood that particles having smaller sizes show superior photocatalytic activity because of the high surface area compared to other samples.[58,59] In addition, as the size of the nanocatalyst increases, the nanocatalyst becomes negatively charged (which is shown in Fig. S2(a)–(c)†), which corresponds to electrostatic repulsion between MB and the catalyst, therefore the PCD efficiency decreases.[5]

Reusability and stability studies

Both catalyst reusability and catalytic efficiency of a catalyst are important parameters for photocatalysis applications. A catalyst is regarded as effective if it can be retrieved and reused while keeping its efficiency intact. Ni–Zn ferrite nanoparticles can be easily recovered with the help of a strong magnet due to their magnetic nature and by centrifugation; they can also be recaptured smoothly. After the successful recovery of the catalyst, the reusability test was performed. The recovered nanocatalyst was utilized to degrade MB dye simultaneously five times for testing the effectiveness of the material (see Fig. S8 in the ESI†). Entire solutions were centrifuged to separate out the photocatalyst after each cycle. After that, de-ionized water was used to wash the isolated nanoparticles three times. On each cycle, the recaptured nanoparticles were added to a new batch of MB solution. This data demonstrates that 90.8% of the MB molecules were still degraded after five successive cycles using the ZNF-1 nanocatalyst as shown in Fig. 8(B), indicating that the catalytic performance of Ni–Zn ferrite nanocatalysts was not considerably altered. The material loss that occurred during the washing processes may be responsible for the observed decrease in photodegradation efficiency. This material loss may be reduced by retrieving from the medium using an external strong magnetic bar. So, for prolonged operation, this is a promising method having both stability and probability.

Study of XRD patterns before and after adsorption

Fig. S9 (in the ESI†) shows the powder XRD patterns of the ZNF-1 nanocatalyst recorded at RT before and after adsorption. No significant change in the diffracted peak position of the ZNF-1 sample was observed before and after adsorption. All the appeared peaks in diffractograms were marked with their Miller indices. As per the obtained XRD result of the ZNF-1 nanocatalyst, the crystal structure of the sample did not change before and after adsorption. The cubic spinel crystallographic phase remains unaltered.

FESEM analysis before and after adsorption

Fig. 9(a)–(d) illustrate the FESEM images of the ZNF-1 nanocatalyst before and after adsorption together with EDS spectra. The presence of homogeneous nanosized particles within the fabricated sample was validated by the FESEM images. There was no notable change in the surface morphology of the ZNF-1 nanocatalyst before and after adsorption as noticed in the FESEM images. The EDS spectra of the ZNF-1 sample also verified the existence of Fe, Ni, Zn and O elements. The obtained percentage of all the elements was found to be in excellent agreement with the calculated value. Non-existence of any foreign elements other than Fe, Ni, Zn and O in the samples also confirmed that the synthesized nanocatalyst is extremely pure.

Photocatalytic degradation mechanism

In the past two decades, several conducted investigations have supported the superiority of spinel ferrite nanoparticles (SFNPs) and spinel ferrite nanocomposites (SFNCs) in the management of water and wastewater. These SFNPs can be readily produced, are stable, and repeatedly used without losing any of their unique properties, which lowers the cost of treatment. Moreover, spinel ferrites are advantageous materials for photocatalytic activity due to their comparatively narrow band gap (~2.0 eV). Nanoferrites can be used only in combination with

© 2023 The Author(s). Published by the Royal Society of Chemistry

Open Access Article. Published on 25 August 2023. Downloaded on 2/6/2026 1:27:51 PM.
This article is licensed under a Creative Commons Attribution-NonCommercial 3.0 Unported Licence.

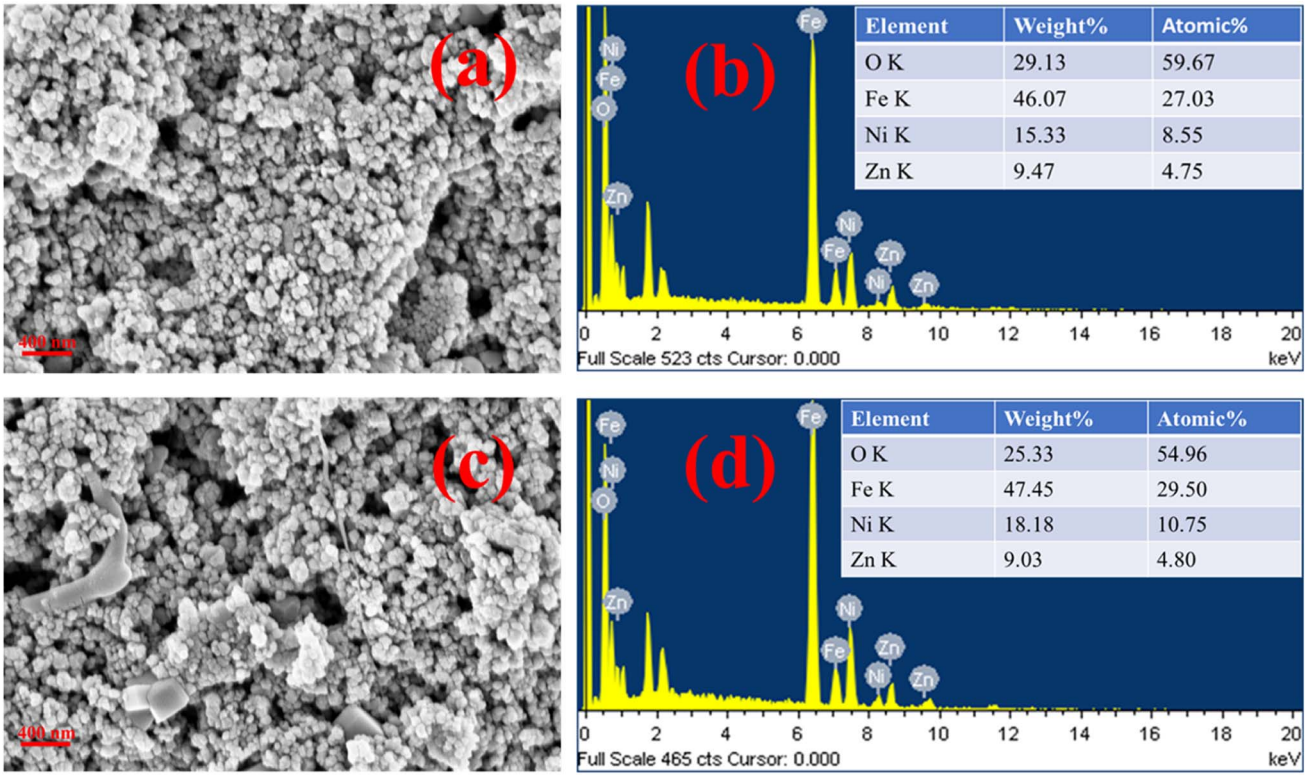

Fig. 9 FESEM images along with EDS of the ZNF-1 nanocatalyst (a and b) before adsorption and (c and d) after adsorption.

other photocatalysts, and with some oxidants, such as H_2O_2, during the photocatalytic investigation.[60–63] A Fenton-type system is made by merging ferrites with H_2O_2 under xenon light exposure or in dark environments that produce the hydroxyl radicals heading to an enhancement in the degradation process. Fenton's reagent, ferrous ions and a homogeneous solution of hydrogen peroxide (H_2O_2), acts as a strong oxidant and causes the generation of hydroxyl radicals ($^{\bullet}OH$). These produced $^{\bullet}OH$ radicals have the potential (2.84 V *versus* the standard hydrogen electrode) to oxidize the organic pollutants present in wastewater. Light is a key factor in improving the degradation effectiveness in a photo-Fenton process for the removal of different organic contaminants from water. Normally, photocatalysts use light energy ($h\nu$) to produce oxidation and reduction reactions. The plausible photocatalytic mechanism of spinel Ni–Zn ferrite nanoparticles is shown through a schematic diagram in Fig. 10.

Spinel Ni–Zn ferrite samples absorb sufficient energy when exposed to xenon light to excite the electrons from the valence band to the conduction band, causing the generation of free electrons (e^-) in the conduction band and holes (h^+) in the valence band.[64,65] The free electrons may be released into the

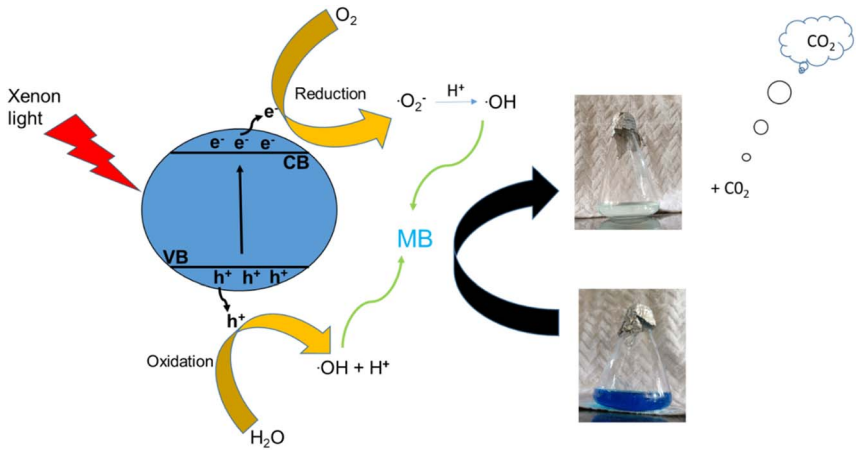

Fig. 10 Schematic diagram of the degradation mechanism.

Open Access Article. Published on 25 August 2023. Downloaded on 2/6/2026 1:27:51 PM. This article is licensed under a Creative Commons Attribution-NonCommercial 3.0 Unported Licence.

dye's aqueous solution, where they interact with the dissolved oxygen to form superoxide radicals (O^{2-}). They can also attack hydroxyl ions or water molecules to produce reactive hydroxide ions ($^{\bullet}OH$), which may have the capability to attack the dye molecules.[66–70] Holes (h^+) in the valence band, meanwhile, can also promote the formation of $^{\bullet}OH$ radicals. As a result, MB can break down into harmless degradation products, including CO_2 and H_2O. Fig. 10 depicts the photocatalytic mechanism used to degrade methylene blue using xenon light. This figure also revealed the resulting changes in the MB solution. The reactions associated with the photocatalytic activity are those that produce hydroxyl radicals as follows

$$Fe^{2+} + H_2O_2 \rightarrow {}^{\bullet}OH + Fe^{3+} + OH^-$$

$$Fe^{3+} + H_2O_2 \rightarrow Fe^{2+} + 2{}^{\bullet}OH + H^+$$

$$Fe^{2+} + {}^{\bullet}OH \rightarrow Fe^{3+} + OH^-$$

Additionally, because of the exposure to xenon light, the degradation process is increased as

$$H_2O_2 + h\nu \rightarrow {}^{\bullet}OH + {}^{\bullet}OH$$

$$Fe^{3+} + H_2O + h\nu \rightarrow Fe^{2+} + {}^{\bullet}OH + H^+$$

Furthermore, the photocatalytic mechanism for methylene blue degradation is a safe process. The hydrogen peroxide used in this process is harmless, easy to handle, and has no dangerous environmental effects because it produces carbon dioxide and water. The reactions that participated in this process are

$$\text{Pollutant} + H_2O_2 \xrightarrow{Fe^{2+} \text{ or } Fe^{3+}} \text{Intermediate}$$

$$\text{Intermediate} + H_2O_2 \xrightarrow{Fe^{2+} \text{ or } Fe^{3+}} CO_2 + H_2O_2 + \text{Inorganic salt}$$

As a result, Ni–Zn ferrite nanoparticles can be utilized to remediate water effectively without harming the environment.

Study of antioxidant properties

Antioxidants are compounds that have the ability to neutralize and scavenge free radicals which may protect cells against free radicals. We have investigated the antioxidant properties of the as-synthesized Ni–Zn ferrite nanoparticles. For this purpose, the DPPH solution that contains stable free radicals was used. The prepared DPPH solution was left undisturbed for 24 hours to verify its stability. Analyzing UV-vis spectra, it was noticed that neither the color nor the strength of the absorption

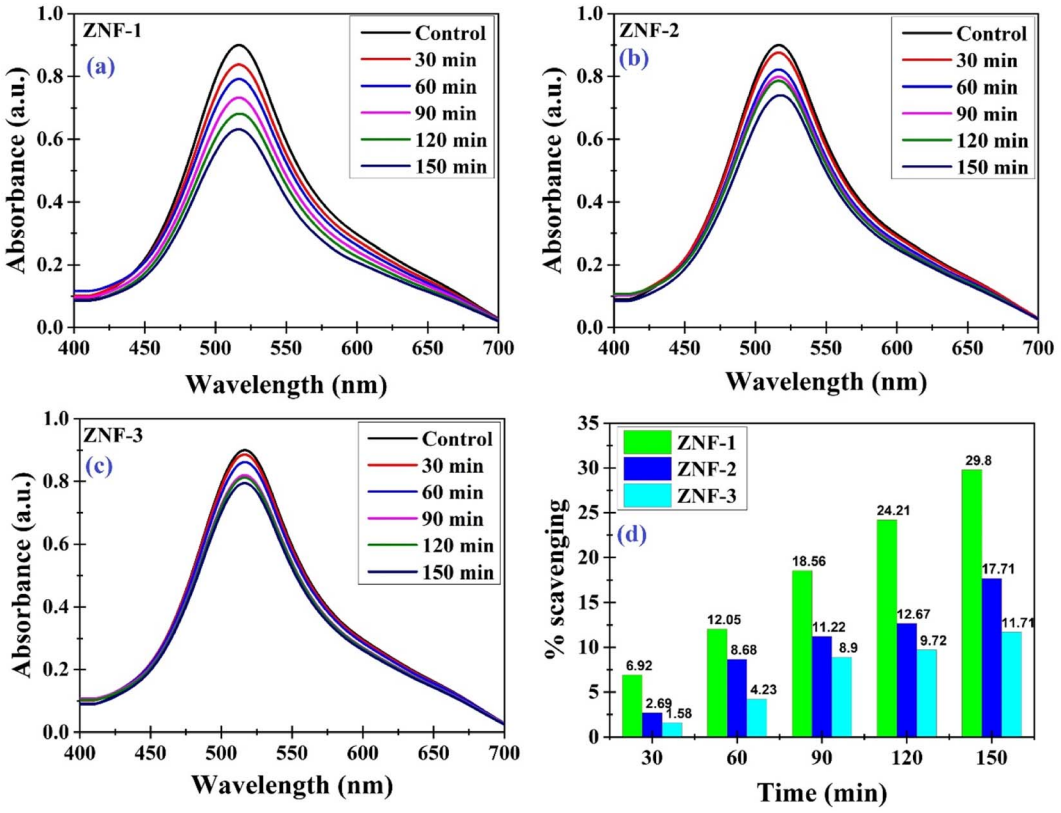

Fig. 11 (a–c) Antioxidant activity recorded at different time intervals for ZNF-1, ZNF-2 and ZNF-3 samples and (d) percentage of scavenging activity of all the Ni–Zn ferrite samples.

© 2023 The Author(s). Published by the Royal Society of Chemistry

Open Access Article. Published on 25 August 2023. Downloaded on 2/6/2026 1:27:51 PM. This article is licensed under a Creative Commons Attribution-NonCommercial 3.0 Unported Licence.

changed at 517 nm, indicating that the DPPH solution was steady throughout the experiment.[25,26] Fig. 11(a)–(c) show the antioxidant activity of all the samples recorded at different time intervals.

The stable nitrogen free radical in the DPPH solution was reduced in the presence of Ni–Zn ferrite nanoparticles, resulting in a notable drop in absorbance measured at 517 nm. Electron transfer from the oxygen atom to the nitrogen atom in DPPH may result in an observed reduction in the intensity of the n* transition at 517 nm. Therefore a gradual change in the color of the DPPH solution was noticed from deep violet towards pale yellow (see Fig. S10, ESI†) which is due to the antioxidant properties of Ni–Zn ferrite nanoparticles.[71] As seen from Fig. 11(d), the ZNF-1 sample having the smallest sized nanoparticles exhibited 29.8% scavenging of free radicals in 150 minutes which is comparatively higher than the other two samples. With increasing particle size, a systematic decrement in the scavenging of free radicals was noticed.

Conclusion

In brief, an explicit study of the size dependent photocatalytic and antioxidant properties of $Zn_{0.3}Ni_{0.7}Fe_2O_4$ nanoparticles has been demonstrated in this article. The standard chemical co-precipitation technique was utilized to synthesize three sets of ferrite nanoparticles with different sizes calcined at various temperatures (400 °C, 600 °C and 800 °C). Investigation of the X-ray diffraction patterns of all three samples confirmed the presence of a single-phase spinel cubic structure. Mean crystallite sizes and generated microstrain inside the tiny crystals were obtained using W–H plots. The microstrain that existed in nanocrystals was found to be of tensile nature. A cautious overview of HRTEM images signified that the prepared nanoparticles were almost spherical shaped and good homogeneity in both size and shape was attained. An excellent match between the average particle size and mean crystallite sizes obtained from W–H graphs was observed. SAED pattern proved the existence of interpenetrating face-centred cubic (FCC) lattices inside the spinel cubic crystal structure Tauc plots of ferrite nanoparticles revealed a gentle decrement in the values of the indirect band gap with increasing mean size. Superparamagnetism in the ferrite samples containing the smallest sized nanoparticles was found at 300 K which is verified by the M–T curves. Magnetic hysteresis loops obtained at both room temperature and 5 K showed an enhancement trend with increasing mean sizes of nanoparticles. Various magnetic parameters such as coercivity, remanence ratio, magnetic moment and effective anisotropy constant for all the samples have been investigated thoroughly. Zeta potentials were measured to compute the stability of nanoparticles in an aqueous solution. FTIR spectra were obtained to understand the nature of chemical bonds in the compounds. For photocatalytic applications of nanoparticles, the porous structure, specific surface area, pore size and total pore volumes associated with them were evaluated using adsorption/desorption isotherms. Photodegradation of MB using ferrite nanocatalysts was examined under the illumination of xenon radiation. Smallest-sized nanoparticles were recognized as eminent photocatalysts because of their high efficiency in reducing MB dye in comparison to others. In the pH-dependent photodegradation studies, ferrite samples consisting of smallest-sized magnetic nanoparticles also performed well and showed high efficiency in an acidic medium. Dye degradation efficiency was noted to reduce with increasing mean particle size. In this work, an attempt was also made to thoroughly investigate the role of active species taking part in dye degradation. The antioxidant qualities of Ni–Zn ferrite nanoparticles were also explored and explained properly. The ZNF-1 sample having the smallest sized nanoparticles exhibited comparatively high scavenging of free radicals in the DPPH solution. Based on this study, it is understood that both the photocatalytic and antioxidant properties of spinel Ni–Zn ferrite nanoparticles depend on the size and the smallest-sized nanoparticles show high efficiency. It is also noted that the photodegradation process using these nanoparticles also actively depends upon the pH of the solution. These synthesized nanomaterials are also extremely useful for low-cost wastewater treatment.

Author contributions

NJM: methodology, investigation, formal analysis, discussion, writing the original draft, and writing – review and editing. RS: methodology, formal analysis. BB: methodology, formal analysis. MPG: conceptualization, methodology, resources, supervision, discussion, writing a part of the original draft, and writing – review and editing. DC: conceptualization, methodology, validation, resources, supervision, discussion, and writing – review and editing.

Conflicts of interest

The authors declare no competing financial interest.

Acknowledgements

NJM thanks CSIR, New Delhi for fellowship, RS thanks UGC, New Delhi for fellowship and BB thank CSIR, New Delhi for fellowship. The authors thank IASST, Guwahati for the in-house project. The authors also thank SAIC-IASST for providing instrumental facilities. All the authors are also thankful to IISER Bhopal and IIT Guwahati for providing magnetic data for samples.

References

1 M. Sundararajan, V. Sailaja, L. John Kennedy and J. Judith Vijaya, *Ceram. Int.*, 2017, **43**, 540–548.
2 A. Makofane, D. E. Motaung and N. C. Hintsho-Mbita, *Ceram. Int.*, 2021, **47**, 22615–22626.
3 S. A. Jadhav, S. B. Somvanshi, M. V. Khedkar, S. R. Patade and K. M. Jadhav, *J. Mater. Sci.: Mater. Electron.*, 2020, **31**, 11352–11365.
4 J. Hammouche, M. Gaidi, S. Columbus and M. Omari, *J. Inorg. Organomet. Polym. Mater.*, 2021, **31**, 3496–3504.

Open Access Article. Published on 25 August 2023. Downloaded on 2/6/2026 1:27:51 PM. This article is licensed under a Creative Commons Attribution-NonCommercial 3.0 Unported Licence.

5 G. Padmapriya, A. Manikandan, V. Krishnasamy, S. K. Jaganathan and S. A. Antony, *J. Mol. Struct.*, 2016, **1119**, 39–47.
6 S. Singhal, R. Sharma, C. Singh and S. Bansal, *Indian J. Eng. Mater. Sci.*, 2013, **2013**, 1–6.
7 K. K. Kefeni and B. B. Mamba, *Sustainable Mater. Technol.*, 2020, **23**, e00140.
8 R. Suresh, S. Rajendran, P. S. Kumar, D.-V. N. Vo and L. Cornejo-Ponce, *Chemosphere*, 2021, **274**, 129734.
9 A. R. Malik, M. H. Aziz, M. Atif, M. S. Irshad, H. Ullah, T. N. Gia, H. Ahmed, S. Ahmad and T. Botmart, *J. Saudi Chem. Soc.*, 2022, **26**, 101422.
10 H. Q. Alijani, S. Iravani, S. Pourseyedi, M. Torkzadeh-Mahani, M. Barani and M. Khatami, *Sci. Rep.*, 2021, **11**, 17431.
11 S. Kanagesan, M. Hashim, S. AB Aziz, I. Ismail, S. Tamilselvan, N. Alitheen, M. Swamy and B. Purna Chandra Rao, *Appl. Sci.*, 2016, **6**, 184.
12 M. P. Ghosh and S. Mukherjee, *J. Am. Ceram. Soc.*, 2019, **102**, 7509–7520.
13 M. P. Ghosh, S. Datta, R. Sharma, K. Tanbir, M. Kar and S. Mukherjee, *Mater. Sci. Eng., B*, 2021, **263**, 114864.
14 J. Gogoi and D. Chowdhury, *Mater. Adv.*, 2023, **4**, 2088–2098.
15 N. J. Mondal, R. Sonkar, S. Thakur, N. C. Adhikary and D. Chowdhury, *ACS Appl. Nano Mater.*, 2023, **6**, 7351–7363.
16 M. P. Ghosh and S. Mukherjee, *J. Magn. Magn. Mater.*, 2019, **489**, 165320.
17 S. B. Darling and S. D. Bader, *J. Mater. Chem.*, 2005, **15**, 4189.
18 Aakash, P. Nordblad, R. Mohan and S. Mukherjee, *J. Magn. Magn. Mater.*, 2017, **441**, 710–717.
19 R. Mohan, M. P. Ghosh and S. Mukherjee, *J. Magn. Magn. Mater.*, 2018, **458**, 193–199.
20 C. Singh, S. Jauhar, V. Kumar, J. Singh and S. Singhal, *Mater. Chem. Phys.*, 2015, **156**, 188–197.
21 M. Gaidi, K. Daoudi, S. Columbus, A. Hajjaji, M. A. E. Khakani and B. Bessais, *J. Environ. Sci.*, 2021, **101**, 123–134.
22 N. D. Raskar, D. V. Dake, V. A. Mane, E. Stathatos, U. Deshpande and B. Dole, *J. Mater. Sci.: Mater. Electron.*, 2019, **30**, 10886–10899.
23 M. Fu, Y. Li, S. Wu, P. Lu, J. Liu and F. Dong, *Appl. Surf. Sci.*, 2011, **258**, 1587–1591.
24 D. Das, B. C. Nath, P. Phukon, A. Kalita and S. K. Dolui, *Colloids Surf., B*, 2013, **111**, 556–560.
25 D. Das, B. C. Nath, P. Phukon and S. K. Dolui, *Colloids Surf., B*, 2013, **101**, 430–433.
26 X. Ge, Z. Cao and L. Chu, *Antioxidants*, 2022, **11**, 791.
27 Aakash, R. Choubey, D. Das and S. Mukherjee, *J. Alloys Compd.*, 2016, **668**, 33–39.
28 R. Sharma, P. Thakur, M. Kumar, P. B. Barman, P. Sharma and V. Sharma, *Ceram. Int.*, 2017, **43**, 13661–13669.
29 V. D. Mote, Y. Purushotham and B. N. Dole, *J. Theor. Appl. Phys.*, 2012, **6**, 6.
30 M. P. Ghosh and S. Mukherjee, *Mater. Res. Bull.*, 2020, **125**, 110785.
31 V. K. Lakhani, T. K. Pathak, N. H. Vasoya and K. B. Modi, *Solid State Sci.*, 2011, **13**, 539–547.
32 K. M. Batoo, *J. Phys. Chem. Solids*, 2011, **72**, 1400–1407.
33 M. Zhang, Z. Zi, Q. Liu, P. Zhang, X. Tang, J. Yang, X. Zhu, Y. Sun and J. Dai, *Adv. Mater. Sci. Eng.*, 2013, **2013**, 1–10.
34 M. Meinert and G. Reiss, *J. Phys.: Condens. Matter*, 2014, **26**, 115503.
35 B. S. Holinsworth, D. Mazumdar, H. Sims, Q.-C. Sun, M. K. Yurtisigi, S. K. Sarker, A. Gupta, W. H. Butler and J. L. Musfeldt, *Appl. Phys. Lett.*, 2013, **103**, 082406.
36 S. Singhal, S. Bhukal, J. Singh, K. Chandra and S. Bansal, *J. Nanotechnol.*, 2011, **2011**, 1–6.
37 Q.-C. Sun, H. Sims, D. Mazumdar, J. X. Ma, B. S. Holinsworth, K. R. O'Neal, G. Kim, W. H. Butler, A. Gupta and J. L. Musfeldt, *Phys. Rev. B: Condens. Matter Mater. Phys.*, 2012, **86**, 205106.
38 D. Carta, M. F. Casula, A. Falqui, D. Loche, G. Mountjoy, C. Sangregorio and A. Corrias, *J. Phys. Chem. C*, 2009, **113**, 8606–8615.
39 S. Kumar, V. Singh, S. Aggarwal, U. K. Mandal and R. K. Kotnala, *Mater. Sci. Eng., B*, 2010, **166**, 76–82.
40 K. S. Ramakrishna, C. Srinivas, C. L. Prajapat, S. S. Meena, M. V. K. Mehar, D. M. Potukuchi and D. L. Sastry, *Ceram. Int.*, 2018, **44**, 1193–1200.
41 M. Zheng, X. C. Wu, B. S. Zou and Y. J. Wang, *J. Magn. Magn. Mater.*, 1998, **183**, 152–156.
42 K. Tanbir, M. P. Ghosh, R. K. Singh, M. Kar and S. Mukherjee, *J. Mater. Sci.: Mater. Electron.*, 2019, **31**, 435–443.
43 M. Zhang, Z. Zi, Q. Liu, P. Zhang, X. Tang, J. Yang, X. Zhu, Y. Sun and J. Dai, *Adv. Mater. Sci. Eng.*, 2013, **2013**, 1–10.
44 P. Thakur, R. Sharma, V. Sharma, P. B. Barman, M. Kumar, D. Barman, S. C. Katyal and P. Sharma, *J. Magn. Magn. Mater.*, 2017, **432**, 208–217.
45 S. J. Kelly, X. Wen, D. P. Arnold and J. S. Andrew, *AIP Adv.*, 2016, **6**, 056105.
46 A. M. Ilosvai, D. Dojcsak, C. Váradi, M. Nagy, F. Kristály, B. Fiser, B. Viskolcz and L. Vanyorek, *Int. J. Mol. Sci.*, 2022, **23**, 5081.
47 H. A. Alhadlaq, M. J. Akhtar and M. Ahamed, *Cell Biosci.*, 2015, **5**, 55.
48 Q. Yu, Y. Su, R. Tursun and J. Zhang, *RSC Adv.*, 2019, **9**, 13173–13181.
49 G. Katoch, J. Prakash, R. Jasrotia, A. Verma, R. Verma, S. Kumari, T. Ahmad, S. K. Godara, J. Ahmed, A. Kandwal, M. Fazil, P. K. Maji, S. Kumar and G. Kumar, *J. Water Process. Eng.*, 2023, **53**, 103726.
50 R. Jasrotia, Suman, A. Verma, R. Verma, J. Ahmed, S. K. Godara, G. Kumar, A. Mehtab, T. Ahmad and S. Kalia, *J. Water Process. Eng.*, 2022, **48**, 102865.
51 O. K. Nimisha, M. Akshay, S. Mannya and A. P. Reena Mary, *Mater. Today: Proc.*, 2022, **66**, 2370–2373.
52 P. Dhiman, G. Rana, E. A. Dawi, A. Kumar, G. Sharma, A. Kumar and J. Sharma, *Water*, 2023, **15**, 187.
53 D. Chahar, D. Kumar, P. Thakur and A. Thakur, *Mater. Res. Bull.*, 2023, **162**, 112205.
54 J. Liu and Z. B. Xu, *Adv. Mater. Res.*, 2012, **472–475**, 157–160.
55 S. S. Mandal and A. J. Bhattacharyya, *J. Chem. Sci.*, 2012, **124**, 969–978.

© 2023 The Author(s). Published by the Royal Society of Chemistry

Open Access Article. Published on 25 August 2023. Downloaded on 2/6/2026 1:27:51 PM.
This article is licensed under a Creative Commons Attribution-NonCommercial 3.0 Unported Licence.

56 V. Mirkhani, S. Tangestaninejad, M. Moghadam, M. H. Habibi and A. Rostami-Vartooni, *J. Iran. Chem. Soc.*, 2009, **6**, 578–587.
57 M. B. Suwarnkar, R. S. Dhabbe, A. N. Kadam and K. M. Garadkar, *Ceram. Int.*, 2014, **40**, 5489–5496.
58 G. Mathubala, A. Manikandan, S. Arul Antony and P. Ramar, *Nanosci. Nanotechnol. Lett.*, 2016, **8**, 375–381.
59 B. Chethan, Y. T. Ravikiran, S. C. Vijayakumari, H. G. Rajprakash and S. Thomas, *Sens. Actuators, A*, 2018, **280**, 466–474.
60 J. Wei, C. Zhang and Z. Xu, *Mater. Res. Bull.*, 2012, **47**, 3513–3517.
61 S. Sun, X. Yang, Y. Zhang, F. Zhang, J. Ding, J. Bao and C. Gao, *Prog. Nat. Sci.: Mater. Int.*, 2012, **22**, 639–643.
62 S.-Q. Liu, L.-R. Feng, N. Xu, Z.-G. Chen and X.-M. Wang, *Chem. Eng. J.*, 2012, **203**, 432–439.
63 D. Chahar, S. Taneja, S. Bisht, S. Kesarwani, P. Thakur, A. Thakur and P. B. Sharma, *J. Alloys Compd.*, 2021, **851**, 156878.
64 P. Dhiman, Mu. Naushad, K. M. Batoo, A. Kumar, G. Sharma, A. A. Ghfar, G. Kumar and M. Singh, *J. Cleaner Prod.*, 2017, **165**, 1542–1556.
65 G. Sharma, A. Kumar, S. Sharma, A. H. Al-Muhtaseb, Mu. Naushad, A. A. Ghfar, T. Ahamad and F. J. Stadler, *Sep. Purif. Technol.*, 2019, **211**, 895–908.
66 H. R. Rajabi, F. Karimi, H. Kazemdehdashti and L. Kavoshi, *J. Photochem. Photobiol., B*, 2018, **181**, 98–105.
67 H. R. Rajabi, H. Arjmand, H. Kazemdehdashti and M. Farsi, *J. Environ. Chem. Eng.*, 2016, **4**, 2830–2840.
68 A. Mehtab, S. Banerjee, Y. Mao and T. Ahmad, *ACS Appl. Mater. Interfaces*, 2022, **14**, 44317–44329.
69 S. A. Ali and T. Ahmad, *Int. J. Hydrogen Energy*, 2022, **47**, 29255–29283.
70 S. A. Ali and T. Ahmad, *Mater. Today Chem.*, 2023, **29**, 101387.
71 B. Jyothish and J. Jacob, *Chem. Phys.*, 2023, **6**, 100209.

© 2023 The Author(s). Published by the Royal Society of Chemistry